Editors' Suggestion

General time-dependent configuration-interaction singles. I. Molecular case

Stefanos Carlström,[1,2,*] Michael Spanner,[3] and Serguei Patchkovskii[1]
[1]*Max-Born-Institut, Max-Born-Straße 2A, 12489 Berlin, Germany*
[2]*Department of Physics, Lund University, Box 118, 22100 Lund, Sweden*
[3]*National Research Council Canada, 100 Sussex Drive, Ottawa, Ontario, Canada K1A 0R6*

(Received 26 April 2022; accepted 8 September 2022; published 10 October 2022)

We present a grid-based implementation of the time-dependent configuration-interaction singles method suitable for computing the strong-field ionization of small gas-phase molecules. After outlining the general equations of motion used in our treatment of this method, we present example calculations of strong-field ionization of He, LiH, H_2O, and C_2H_4 that demonstrate the utility of our implementation. The following paper [S. Carlström *et al.*, following paper, Phys. Rev. A **106**, 042806 (2022)] specializes to the case of spherical symmetry, which is applied to various atoms.

DOI: 10.1103/PhysRevA.106.043104

I. INTRODUCTION

Strong-field physics and attosecond science offer a rich experimental platform to study ultrafast phenomena on electronic timescales and length scales [1,2]. Applied to gas phase molecules, techniques such as high-harmonic spectroscopy [3–7], orbital tomography [8], laser-induced electron diffraction [9–11], and holography [12] attempt to use the technologies of attosecond physics to probe electronic structures and dynamics that occur within molecular systems. Although promising, fine-tuning these techniques to extract accurate and complete information is not straightforward due to the highly nonlinear and nonperturbative nature of the strong-field interactions driving these experimental efforts. Often the only path to disentangling and interpreting the measurable experimental observables is through detailed modeling of not only the underlying molecular and electronic structures but also the complete probing process itself. In this regard, the novel spectroscopic methods brought forth by strong-field and attosecond physics will only be as accurate as the underlying modeling used to interpreting the complex observables involved.

The first step in all of these strong-field driven processes is the removal of an electron with a strong low-frequency laser field. Following ionization, the liberated electron is then accelerated in the laser field and driven back to recollide with the parent ion, a process called laser-induced electron recollision. In order to accurately describe this time-dependent nonperturbative process at an *ab initio* level, it is necessary to develop time-domain methods that can interface with standard methods in time-independent electronic structure theory. In addition, a proper description of the recollision motion of the continuum electron will likely require going beyond the localized Gaussian-like basis sets upon which most of standard electronic structure codes are based. In this article we develop and explore a grid-based implementation of time-dependent configuration-interaction singles (TD-CIS) as applied to small gas-phase molecules, where Cartesian grids are used to represent the continuum electron, while still using Gaussians for the occupied orbitals.

The problems we are interested in studying are not new, and many different approaches have been fruitfully pursued before. A listing, which is by no means exhaustive, would include TD-CIS for molecules [13–19]; TD-CIS for atoms [20,21]; a newly developed relativistic TD-CIS that takes the Dirac equation as its starting point [22]; time-dependent density-functional theory [23–26]; methods that go beyond the single Slater determinant ansatz, such as multiconfigurational time-dependent Hartree [27–29], multiconfigurational time-dependent Hartree–Fock [30–34], and time-dependent multiconfigurational self-consistent-field methods [35]; time-dependent complete-active-space self-consistent-field methods [36]; time-dependent resolution in ionic states [37]; the various restricted-active-space methods, e.g., time-dependent restricted-active-space configuration-interaction [38] and time-dependent occupation-restriction multiple-active-space methods [39]; the excitation-class-based methods such as time-dependent coupled-cluster [40–42] and algebraic diagrammatic construction [43–45]; and finally the recent extension of the *R*-matrix method to molecules, UKRmol+ [46] and RMT [47]. For reviews of the various *ab initio* approaches to multielectron dynamics, see [48,49].

This article is arranged as follows. In Sec. II the general equations of motion for the TD-CIS ansatz are derived in detail, as well as the generalization of surface-flux techniques to compute photoelectron spectra to multiple ionization channels. The time propagator is briefly surveyed in Sec. III. Some illustrative calculations are presented in Sec. IV. Section V concludes the paper.

*stefanos@mbi-berlin.de, stefanos.carlstrom@matfys.lth.se

A. Conventions

Hartree atomic units, where $\hbar = e = a_0 = m_e = 1$, are used throughout.

We employ a modified version of Einstein's summation convention, where indices appearing on one side of an equality sign only are automatically contracted over, e.g.,

$$\Psi = c_0\Phi_0 + \tilde{\Phi}_k \equiv c_0\Phi_0 + \sum_k \tilde{\Phi}_k.$$

For the canonical orbitals, we use the following letters: $|i\rangle$, $|j\rangle$, $|k\rangle$, and $|l\rangle$ denote occupied orbitals; $|a\rangle$ and $|b\rangle$ denote virtual orbitals; and $|c\rangle$, $|d\rangle$, $|e\rangle$, and $|f\rangle$ denote *any* orbitals. Matrix elements between orbitals are written using Mulliken-like notation:

$$\begin{aligned}(c|d) &\stackrel{\text{def}}{=} \langle c|\hat{h}_0 + \hat{V}_L(t)|d\rangle,\\ [cd||ef] &\stackrel{\text{def}}{=} [cd|ef] - [cd|fe],\\ [cd|ef] &\stackrel{\text{def}}{=} \int \frac{d\varsigma_1 d\varsigma_2}{|\mathbf{r}_1 - \mathbf{r}_2|}\chi_c^*(\varsigma_1)\chi_d^*(\varsigma_2)\chi_e(\varsigma_1)\chi_f(\varsigma_2),\end{aligned} \quad (1)$$

where $\hat{h}_0 \stackrel{\text{def}}{=} \hat{T} + \hat{V}$ is the molecular one-body Hamiltonian, $\hat{V}_L(t)$ is the time-dependent potential due to the external laser field, and $\varsigma_{1,2}$ refer to both spatial and spin coordinates of the orbitals.

II. GENERAL TD-CIS, EQUATIONS, AND SURFACE FLUX

Our ansatz is

$$\Psi(t) = c_0(t)\Phi_0 + \tilde{\Phi}_k(t), \quad (2)$$

where Φ_0 is the Slater determinant of the reference state [typically the Hartree–Fock (HF) ground state], $c_0(t)$ is time-dependent complex amplitude, and $\tilde{\Phi}_k(t)$ an excited Slater determinant obtained by substituting the occupied orbital $|k\rangle$ of the reference by a time-dependent particle orbital $|\tilde{k}\rangle$ formed as a linear combination of the virtual canonical orbitals:

$$\tilde{\Phi}_k(t) \stackrel{\text{def}}{=} c_{ka}(t)\hat{a}_a^\dagger\hat{a}_k\Phi_0 \Rightarrow |\tilde{k}\rangle = c_{ka}(t)|a\rangle.$$

No distinction is made between excitation and ionization channels, since $|\tilde{k}\rangle$ is associated with a particular hole configuration of the remaining ion, the particle–hole density of which is given by $|\tilde{k}\rangle\langle k|$. We also note that this implies that particle orbitals corresponding to different occupied orbitals are nonorthogonal, $\langle\tilde{k}|\tilde{l}\rangle \neq 0$, which must be taken into account when forming the energy expression [50].

To derive the equations of motion (EOMs), we start from the Dirac–Frenkel variational principle

$$\delta_{\langle\Psi|}\hat{L} = 0, \quad (3)$$

where the Lagrangian is given by

$$\hat{L} = \langle\Psi|\hat{H} - i\partial_t|\Psi\rangle - \lambda_{i\tilde{j}}\langle i|\tilde{j}\rangle - \lambda_{\tilde{j}i}\langle\tilde{j}|i\rangle. \quad (4)$$

The Lagrange multipliers $\lambda_{i\tilde{j}}$ and $\lambda_{\tilde{j}i}$ ensure that the particle orbitals $|\tilde{j}\rangle$ remain orthogonal to the occupied orbitals $|i\rangle$ at all times; this is necessary since otherwise the basis would be overcomplete. In the time propagation, they are implemented as projectors, without explicitly evaluating the multipliers. A possible alternative approach would have been to treat the Lagrange multipliers as dynamical variables [51]. Such a formulation avoids an explicit orthogonalization step, quadratic in the number of orbitals, leading to substantial efficiency improvements in effective one-electron theories such as time-dependent density-functional theory. The potential savings are however likely to remain minor in wave-function-based methods such as TD-CIS.

Inserting the ansatz (2) into the expression (4) for the Lagrangian, we find

$$\hat{L} = E - c_0^* i\partial_t c_0 - \langle\tilde{k}|i\partial_t|\tilde{k}\rangle - \lambda_{i\tilde{j}}\langle i|\tilde{j}\rangle - \lambda_{\tilde{j}i}\langle\tilde{j}|i\rangle, \quad (4')$$

where the total energy is given by

$$\begin{aligned}E = |c_0|^2E_0 + \langle\tilde{k}|\tilde{k}\rangle E_k + (c_0^*E_{k\tilde{k}} + \text{c.c.})\\ + E_{\tilde{k}\tilde{k}} - \langle\tilde{k}|\tilde{l}\rangle E_{lk} - [l\tilde{k}||k\tilde{l}].\end{aligned}$$

We have introduced here the following notation for the partial contributions to the overall energy:

$$E_0 \stackrel{\text{def}}{=} (i|i) + \tfrac{1}{2}[ij||ij]$$

is the (time-dependent) energy of the reference determinant Φ_0,

$$E_k \stackrel{\text{def}}{=} E_0 - \epsilon_k$$

is the channel energy associated with excitation or ionization from the occupied orbital k, and the orbital energy

$$\epsilon_k \stackrel{\text{def}}{=} \epsilon_{kk}, \quad \epsilon_{kl} \stackrel{\text{def}}{=} (k|l) + \tfrac{1}{2}[kj||lj].$$

The occupied–virtual orbital energy (as well as its complex conjugate)

$$E_{k\tilde{k}} \stackrel{\text{def}}{=} (k|\tilde{k}) + [ki||\tilde{k}i]$$

contains the terms that lead to excitation or ionization from the reference, whereas the virtual–virtual energy

$$E_{\tilde{k}\tilde{k}} \stackrel{\text{def}}{=} (\tilde{k}|\tilde{k}) + [\tilde{k}i||\tilde{k}i]$$

describes the interaction of the excited or ionized electron with its parent ion state (intrachannel) as well as with the external field. Finally, the interchannel energies

$$E_{lk} \stackrel{\text{def}}{=} (l|k) + [li||ki]; \quad [l\tilde{k}||k\tilde{l}]$$

describe coupling between the various ionization channels through the external field and Coulomb interaction, respectively. We note that, due to the linearity of the ansatz (2), we are free to choose the energy origin;[1] by setting $E_0 = 0$, we avoid having to converge the quick phase evolution due to the HF reference. Simultaneously, the channel energy becomes simply $E_k = -\epsilon_k$.

By varying (4′) with respect to c_0^* and $\langle\tilde{k}|$, we get the EOMs

$$\begin{aligned}i\partial_t c_0 &= c_0E_0 + \langle k|\hat{f}|\tilde{k}\rangle,\\ i\partial_t|\tilde{k}\rangle &= (E_k + \hat{f})|\tilde{k}\rangle + c_0\hat{f}|k\rangle\\ &\quad - \langle l|\hat{f}|k\rangle|\tilde{l}\rangle - (\hat{J}_{lk} - \hat{K}_{lk})|\tilde{l}\rangle - \lambda_{\tilde{k}i}|i\rangle,\end{aligned} \quad (5)$$

[1] This can be thought of as a gauge transform.

where the Fock operator is defined as

$$\hat{f} \overset{\text{def}}{=} \hat{h}_0 + \hat{V}_L(t) + \hat{J}_{ii} - \hat{K}_{ii} \Rightarrow \langle l|\hat{f}|k\rangle \equiv \epsilon_{lk}$$

and the direct and exchange potentials are defined by their action on an orbital:

$$\hat{J}_{cd}|e\rangle \overset{\text{def}}{=} \chi_e(\varsigma_1)\int \frac{d\varsigma_2}{|\mathbf{r}_1-\mathbf{r}_2|}\chi_c^*(\varsigma_2)\chi_d(\varsigma_2),$$

$$\hat{K}_{cd}|e\rangle \overset{\text{def}}{=} \chi_d(\varsigma_1)\int \frac{d\varsigma_2}{|\mathbf{r}_1-\mathbf{r}_2|}\chi_c^*(\varsigma_2)\chi_e(\varsigma_2) \equiv \hat{J}_{ce}|d\rangle.$$

We now use our gauge freedom to choose $E_0 = 0$ and we get the modified EOMs

$$\begin{aligned} i\partial_t c_0 &= \langle k|\hat{f}|\tilde{k}\rangle, \\ i\partial_t|\tilde{k}\rangle &= (-\langle k|\hat{f}|k\rangle + \hat{f})|\tilde{k}\rangle + c_0\hat{f}|k\rangle \\ &\quad - \langle l|\hat{f}|k\rangle|\tilde{l}\rangle - (\hat{J}_{lk} - \hat{K}_{lk})|\tilde{l}\rangle - \lambda_{\tilde{k}i}|i\rangle. \end{aligned} \tag{5′}$$

If $|k\rangle$ and $|\tilde{k}\rangle$ live in different vector spaces, e.g., if $|k\rangle$ is expanded in a basis set of Gaussians and $|\tilde{k}\rangle$ is resolved on a grid, their respective matrix representations of the Fock operator $\hat{f}$ will in general not agree, i.e., $|k\rangle$ resolved on the grid of $|\tilde{k}\rangle$ will not necessarily be an eigenvector of the matrix representation of $\hat{f}$ on the same grid. It is therefore important to compute matrix elements of operators in the correct vector space. The chief reason for representing the occupied orbitals using Gaussians instead of resolving them on the grid and computing the matrix elements of the Fock operator accordingly is that any grid coarse enough to be reasonable for time propagation would not be able to accurately represent the oscillatory behavior of the Fock operator close to the nuclei. Specifically, the direct interaction $\hat{J}_{ii}$ needs to partially screen the nuclear potentials $-Z_B/|\mathbf{R}_B - \mathbf{r}_i|$ such that the long-range potential behaves as $-1/r_i$. This cancellation is challenging to achieve accurately on a coarse grid, while it is trivial to compute exactly in the Gaussian basis and then instantiate the result on the grid. A similar argument can be made for the short-range nonlocal potential $\hat{J}_{ii} - \hat{K}_{ii}$.

If instead $|k\rangle$ and $|\tilde{k}\rangle$ *do* live in the same vector space, we may choose $|k\rangle, |l\rangle, \ldots$ to be the canonical orbitals which diagonalize the field-free Fock operator. This choice (which we make in the special case of atomic symmetry; see the following article [52]) is a restriction compared to the more general case considered in this article. Furthermore, in the case of an atom placed at the origin of our coordinate system, there are no permanent dipole moments. These two restrictions considerably simplify the EOMs,

$$\begin{aligned} i\partial_t c_0 &= \langle k|\hat{V}_L|\tilde{k}\rangle, \\ i\partial_t|\tilde{k}\rangle &= (-\epsilon_k + \hat{f})|\tilde{k}\rangle + c_0\hat{V}_L|k\rangle \\ &\quad - \langle l|\hat{V}_L|k\rangle|\tilde{l}\rangle - (\hat{J}_{lk} - \hat{K}_{lk})|\tilde{l}\rangle - \lambda_{\tilde{k}i}|i\rangle, \end{aligned} \tag{5″}$$

where we have dropped the term $c_0(\hat{h}_0 + \hat{J}_{ii} - \hat{K}_{ii})|k\rangle$ since we require $\langle k|\tilde{k}\rangle = 0$. Our molecular implementation below uses (5′), while our atomic implementation [52] relies on (5″).

A. t+iSURF{C,V}

The following derivation in similar in spirit to those of Scrinzi [53], Orimo *et al.* [54], but differs in the details.

We begin by defining the N-electron Heaviside function acting on one electron

$$\Theta \overset{\text{def}}{=} \hat{\Pi}_{jN}[1-\theta(r_1 - R_s)]\cdots[1-\theta(r_{N-1} - R_s)]\theta(r_N - R_s), \tag{6}$$

where $\hat{\Pi}_{jN}$ permutes coordinates j and N. With this, we construct our ansatz for the asymptotic region ($r_j > R_s$),

$$\begin{aligned} \Theta|\Psi(t)\rangle &= a_n(\mathbf{p}_{\sigma_z}, t)\mathcal{A}|\xi_n(t)\rangle|\mathbf{p}_{\sigma_z}(t)\rangle \\ &\overset{\text{def}}{=} a_n(\mathbf{p}_{\sigma_z}, t)|\xi_n(t)\mathbf{p}_{\sigma_z}(t)\rangle, \end{aligned}$$

where $\{|\xi_n(t)\rangle\}$ is a "time-dependent, complete but otherwise arbitrary set of functions" [53] that spans the ion degrees of freedom and $|\mathbf{p}_{\sigma_z}(t)\rangle$ is an electron with final momentum $\mathbf{p}$ and spin projection σ_z.

The antisymmetrization operator used above to couple an already antisymmetrized $(N-1)$-body wave function $|\xi_n(t)\rangle$ with one electron $|\mathbf{p}_{\sigma_z}(t)\rangle$ to form an antisymmetrized N-body wave function is defined as

$$\mathcal{A} \overset{\text{def}}{=} \frac{1}{\sqrt{N}}(-)^{N-j}\hat{\Pi}_{jN}, \tag{7}$$

where $(-)^{N-j}$ is the signature of the permutation. This form is valid, provided that the strong orthogonality assumption applies, i.e., that the scattering state $|\mathbf{p}_{\sigma_z}(t)\rangle$ is orthogonal to all the bound orbitals of the initial state [55–58]. This condition is trivially fulfilled due to the presence of the Heaviside function (6).

The overlap with such an asymptotic state is given by

$$\begin{aligned} a_n(\mathbf{p}_{\sigma_z}, t) &= \langle \xi_n(t)\mathbf{p}_{\sigma_z}(t)|\Theta|\Psi(t)\rangle \\ &= \langle \xi_n(t)|\langle \mathbf{p}_{\sigma_z}(t)|\mathcal{A}\Theta|\Psi(t)\rangle \\ &= \langle \mathbf{p}_{\sigma_z}(t)|\theta\sqrt{N}\langle \xi_n(t)|\Psi(t)\rangle\rangle \\ &\overset{\text{def}}{=} \langle \mathbf{p}_{\sigma_z}(t)|\theta|n(t)\rangle, \end{aligned} \tag{8}$$

where we have used the fact that $\mathcal{A}$ is self-adjoint to act with it on $\Theta|\Psi(t)\rangle$ to the right and that only N terms are nonzero for which the coordinate of $|\mathbf{p}_{\sigma_z}(t)\rangle$ coincides with the photoelectron orbital in $|\Psi(t)\rangle$ (a single orbital in TD-CIS). The sign of each such term will precisely compensate the corresponding sign of the antisymmetrizer (7). The normalization leaves a factor of $\sqrt{N}$, which is absorbed into the definition of the Dyson orbital $|n(t)\rangle$. Finally, $\rangle\rangle$ denotes integration over both the photoelectron and ion coordinates. The benefit of formulating the photoelectron amplitudes in terms of Dyson orbitals is that the various surface terms then attain the familiar expressions from the single-electron case, with the Dyson orbital replacing the single-electron wave function. The only remaining difference is in the channel coupling through the ion Hamiltonian.

It is convenient to choose $|\xi_n(t)\rangle$ as the time-dependent eigenstates of the ion,

$$\begin{aligned} |\xi_n(t)\rangle &\overset{\text{def}}{=} e^{-iE_n(t-t_i)}|\xi_n\rangle \\ \Rightarrow \langle \xi_n(t)|[i\partial_t^\dagger + E_n] &\equiv \langle \xi_n(t)|[i\partial_t^\dagger + \hat{H}_{\text{ion}}] = 0, \end{aligned}$$

where t_i is some reference time, usually taken as the beginning of the laser interaction. Similarly, the scattering states obey the

one-electron TDSE

$$\langle \mathbf{p}_{\sigma_z}(t)|[i\partial_t^\dagger + \hat{h}_S] = 0$$

and the wave function in the asymptotic region

$$[i\partial_t - (\hat{H}_{\text{ion}} + \hat{h}_S)]|\Psi(t)\rangle = 0.$$

The EOMs for the overlaps (8) are then

$$\begin{aligned}
-i\partial_t a_n(\mathbf{p}_{\sigma_z}, t) &= \langle \mathbf{p}_{\sigma_z}(t)|\hat{h}_S\theta\sqrt{N}\langle\xi_n(t)|\Psi(t)\rangle\rangle + E_n\langle \mathbf{p}_{\sigma_z}(t)|\theta\sqrt{N}\langle\xi_n(t)|\Psi(t)\rangle\rangle - \langle \mathbf{p}_{\sigma_z}(t)|\theta\sqrt{N}\langle\xi_n(t)|\hat{H}_{\text{ion}}(t) + \hat{h}_S|\Psi(t)\rangle\rangle \\
&= E_n a_n(\mathbf{p}_{\sigma_z}, t) - \langle \mathbf{p}_{\sigma_z}(t)|\theta\sqrt{N}\langle\xi_n(t)|\hat{H}_{\text{ion}}(t)\hat{\mathbf{1}}|\Psi(t)\rangle\rangle + \langle \mathbf{p}_{\sigma_z}(t)|\hat{h}_S\theta - \theta\hat{h}_S|n(t)\rangle \\
&= E_n a_n(\mathbf{p}_{\sigma_z}, t) - \underbrace{\langle\xi_n(t)|\hat{H}_{\text{ion}}(t)|\xi_m(t)\rangle}_{\stackrel{\text{def}}{=}\mathsf{H}_{nm}(t)} \underbrace{\langle \mathbf{p}_{\sigma_z}(t)|\theta|\mathbf{q}_{\sigma_{z'}}(t)\rangle}_{\delta(\mathbf{p}-\mathbf{q})\delta_{\sigma_z\sigma_{z'}}} a_m(\mathbf{q}_{\sigma_{z'}}, t) + \underbrace{\langle \mathbf{p}_{\sigma_z}(t)|[\hat{h}_S, \theta]|n(t)\rangle}_{S_n(\mathbf{p}_{\sigma_z}, t)} \\
&= -\tilde{\mathsf{H}}_{nm}(t)a_m(\mathbf{p}_{\sigma_z}, t) + S_n(\mathbf{p}_{\sigma_z}, t),
\end{aligned}$$

where the ionic Hamiltonian in the interaction picture is given by

$$\begin{aligned}
\tilde{\mathsf{H}}_{nm}(t) &\stackrel{\text{def}}{=} \mathsf{H}_{nm}(t) - \delta_{nm}E_n, \\
\mathsf{H}_{nm}(t) &= \langle\xi_n(t)|\hat{H}_{\text{ion}}(t)|\xi_m(t)\rangle \\
&= e^{iE_{nm}t}[\delta_{nm}E_n + \langle\xi_n|\hat{V}_L(t)|\xi_m\rangle] \\
E_{nm} &= E_n - E_m,
\end{aligned}$$

and the asymptotic resolution of identity by

$$\hat{\mathbf{1}} = |\xi_m(t)\rangle|\mathbf{q}_{\sigma_{z'}}(t)\rangle\langle\mathbf{q}_{\sigma_{z'}}(t)|\langle\xi_m(t)|.$$

The EOMs can be written in matrix form

$$-i\partial_t\mathbf{a}(\mathbf{p}_{\sigma_z}, t) = -\tilde{\mathsf{H}}(t)\mathbf{a}(\mathbf{p}_{\sigma_z}, t) + \mathbf{S}(\mathbf{p}_{\sigma_z}, t). \tag{9}$$

Here $S_n(\mathbf{p}_{\sigma_z}, t)$ is the surface term contributing to ionization channel n and final photoelectron momentum $\mathbf{p}$ and spin projection σ_z. The precise form of the surface terms depends on the asymptotic wave function chosen (e.g., Coulomb or Volkov scattering wave functions), as well as the gauge [59,60].

Rearranging, we get

$$\partial_t\mathbf{a}(\mathbf{p}_{\sigma_z}, t) + i\tilde{\mathsf{H}}(t)\mathbf{a}(\mathbf{p}_{\sigma_z}, t) = i\mathbf{S}(\mathbf{p}_{\sigma_z}, t), \tag{9′}$$

which is an inhomogeneous differential equation for the photoionization amplitude $\mathbf{a}(\mathbf{p}_{\sigma_z}, t)$. If we discretize (9′) in time and apply the trapezoidal rule, evaluating the ionic Hamiltonian at half the time step, we find (suppressing the dependence on $\mathbf{p}_{\sigma_z}$)

$$\begin{aligned}
&\frac{\mathbf{a}_{j+1} - \mathbf{a}_j}{\tau} + \frac{i}{2}(\tilde{\mathsf{H}}_{j+1/2}\mathbf{a}_{j+1} + \tilde{\mathsf{H}}_{j+1/2}\mathbf{a}_j) = \frac{i}{2}(\mathbf{S}_{j+1} + \mathbf{S}_j) \\
&\iff \left(\hat{\mathbf{1}} + \frac{i\tau}{2}\tilde{\mathsf{H}}_{j+1/2}\right)\mathbf{a}_{j+1} \\
&= \left(\hat{\mathbf{1}} - \frac{i\tau}{2}\tilde{\mathsf{H}}_{j+1/2}\right)\mathbf{a}_j + \frac{i\tau}{2}(\mathbf{S}_j + \mathbf{S}_{j+1}),
\end{aligned} \tag{10}$$

which is globally accurate to $O\{\tau^2\}$.

1. Diagonal $\tilde{\mathsf{H}}$

If $\tilde{\mathsf{H}}$ is diagonal (and time independent), its elements are zero, no channel-coupling occurs, and we can integrate each component of (9′) separately,

$$\begin{aligned}
a_n(\mathbf{p}_{\sigma_z}, t) &= i\int_{t_i}^{t} d\tau S_n(\mathbf{p}_{\sigma_z}, \tau) \\
&= i\int_{t_i}^{t} d\tau\langle \mathbf{p}_{\sigma_z}(\tau)|[\hat{h}_S, \theta]|n(\tau)\rangle,
\end{aligned} \tag{11}$$

we recover Koopman's theorem [since $|\xi_n(\tau)\rangle \equiv e^{-iE_n(\tau-t_i)}|\xi\rangle$], which is an excellent approximation in configuration-interaction singles, if promotions are allowed from the valence shell only.

2. iSURF

In the case of a discretized spectrum [61], the time evolution of the wave function after the end of the pulse ($t = t_f$) is trivially given by

$$|\Psi(t > t_f)\rangle = |\gamma\rangle\langle\gamma|\Psi(t_f)\rangle e^{-iE_\gamma(t-t_f)}, \tag{12}$$

where γ represents all quantum numbers necessary to describe an eigenstate of the field-free Hamiltonian $\hat{H}_0$ and E_γ is its eigenenergy, which will have a negative imaginary part in the presence of absorbing boundary conditions (corresponding to exponential decay of outgoing waves). Furthermore, after the pulse has ended, $\tilde{\mathsf{H}}$ is diagonal, i.e., there is no coupling between the ionization channels anymore, and only the surface term remains, and the amplitude is given by (11). Integrating this amplitude from the end of the pulse t_f to the detection time (suppressing the $\mathbf{p}_{\sigma_z}$ argument), we find

$$a_n(\infty) - a_n(t_f) = i\int_{t_f}^{\infty} d\tau\langle \mathbf{p}_{\sigma_z}(\tau)|[\hat{h}_S, \theta]|n(\tau)\rangle.$$

The total amplitude for channel n will be given by

$$\begin{aligned}
a_n(\infty) &= a_n(t_f) + [a_n(\infty) - a_n(t_f)] \\
&= \underbrace{a_n(t_f)}_{\text{tSURFF}} + \underbrace{i\int_{t_f}^{\infty} d\tau S_n(\tau)}_{\text{iSURF}}.
\end{aligned}$$

Inserting the ansatz (12) into the source term, we find

$$\begin{aligned}
S_n\big(\mathbf{p}_{\sigma_z}, t > t_f\big) &= \langle \mathbf{p}_{\sigma_z}(t)|[\hat{h}_S, \theta]|n(t)\rangle \\
&= \langle \mathbf{p}_{\sigma_z}(t)|[\hat{h}_S, \theta]\sqrt{N}\langle\xi_n(t)|\gamma\rangle\langle\gamma|\Psi(t_f)\rangle\rangle \\
&\quad \times e^{i(\epsilon - E_\gamma)(t-t_f)},
\end{aligned}$$

where the target energy is chosen as $\epsilon \stackrel{\text{def}}{=} E_n + p^2/2$. By identical manipulations as in Eqs. (14)–(17) of [60] and assuming the existence of the operator inverse, we arrive at

$$a_n(\infty) - a_n(t_f) = \langle \mathbf{p}_{\sigma_z}(t_f)|[\hat{h}_S, \theta]|n(\epsilon)\rangle, \tag{13}$$

where the Dyson orbital is given by

$$|n(\epsilon)\rangle = \sqrt{N}\langle \xi_n(t_f)|\Omega(\epsilon)\rangle, \quad |\Omega(\epsilon)\rangle \stackrel{\text{def}}{=} (\hat{H}_0 - \epsilon)^{-1}|\Psi(t_f)\rangle,$$

and $|\Omega(\epsilon)\rangle$ is found using GMRES [62], with the one-body Hamiltonian $\hat{h}_0 - \epsilon$ as the preconditioner. We stress that Eqs. (9′), (10), and (13) are valid for single ionization for any ansatz and not just TD-CIS (2).

3. *Surface terms and gauge dependence*

The surface terms require the evaluation of

$$S_n(\mathbf{p}_{\sigma_z}, t) = \langle \mathbf{p}_{\sigma_z}(t)|[\hat{h}_S, \theta]|n(t)\rangle,$$

which depends on the particular form of scattering wave functions chosen, as well as the gauge:

$$\begin{aligned} \hat{h}_S = \hat{T} + \hat{V}_L(t) = \hat{T} + \begin{cases} \mathbf{F}(t)\cdot\mathbf{r} & \text{(length gauge)} \\ \mathbf{A}(t)\cdot\mathbf{p} & \text{(velocity gauge)}, \end{cases} \\ \Rightarrow [\hat{h}_S, \theta] = [\hat{T}, \theta] + \begin{cases} 0 & \text{(length gauge)} \\ [\mathbf{A}(t)\cdot\mathbf{p}, \theta] & \text{(velocity gauge)}. \end{cases} \end{aligned} \tag{14}$$

tSURFF has customarily been used in the velocity gauge, which is valid since the single-active-electron approximation is gauge invariant (provided only local potentials are used) [59,60]. In this gauge, the Volkov scattering wave functions have the simple expression

$$\chi^{\mathrm{V}}_{\mathbf{p}v}(t, \mathbf{r}) = \frac{1}{(2\pi)^{3/2}} \exp\left\{ i\mathbf{p}\cdot\mathbf{r} - \frac{i}{2}\int_{t_0}^{t} dt'[\mathbf{p} + \mathbf{A}(t')]^2 \right\},$$

the spatial part of which can be evaluated prior to time propagation; only the Volkov phase varies with time.

If we instead work in the length gauge, we also need to gauge transform the scattering wave functions according to

$$\begin{aligned} &\chi^{\mathrm{V}}_{\mathbf{p}l}(t, \mathbf{r}) \\ &\quad = \exp[i\mathbf{A}(t)\cdot\mathbf{r}]\chi^{\mathrm{V}}_{\mathbf{p}v}(t, \mathbf{r}) \\ &\quad = \frac{1}{(2\pi)^{3/2}} \exp\left\{ i[\mathbf{p} + \mathbf{A}(t)]\cdot\mathbf{r} - \frac{i}{2}\int_{t_0}^{t} dt'[\mathbf{p} + \mathbf{A}(t')]^2 \right\}, \end{aligned}$$

which means that when solving (10) in the length gauge, the spatial part of the scattering wave functions needs to be reevaluated at every time step. However, as we see in Eq. (14), the laser coupling term in the surface term vanishes.

We note that TD-CIS is *not* gauge invariant [48,63,64] and velocity gauge calculations with fixed bound orbitals cannot be expected to agree with length gauge calculations. Recently, Sato *et al.* [65] introduced a rotated velocity gauge TD-CIS formulation, where the gauge transform from length gauge to velocity gauge is applied to the bound orbitals on the fly.

III. TIME PROPAGATOR

The EOMs (5′) are solved by a simple fourth-order Runge–Kutta propagator, since that only requires the action of the Hamiltonian on the wave function. The action of the direct and exchange potentials on the particle orbitals $|\tilde{k}\rangle$ is computed by solving Poisson's problem via successive overrelaxation [66,67]. The use of iterative solvers means that the computational complexity scales approximately linearly with the number of grid points, which in turn is given by

$$n_g = \kappa n_x n_y n_z n_c, \quad \kappa = \begin{cases} 1 & \text{(spin restricted)} \\ 2 & \text{(spin unrestricted)}, \end{cases}$$

and n_c is the number of channels. Orthogonality of the particle orbitals to the source orbitals is maintained by projecting out the latter from the former, every time the Hamiltonian is applied.

To suppress reflections from the boundary of the computational domain, we use the complex-absorbing potential (CAP) by Manolopoulos [68], with a design parameter $\delta = 0.2$ leading to less than 1% reflection for all momenta above $k_{\min} = 1.5$ a.u. The CAP then spans the last 4.37 bohrs of the box in each direction. To avoid lowering the convergence order of the propagator, the CAP is multiplied by the time step and applied as a mask function, separately from the other terms in the Hamiltonian. The reason for this is that the convergence of the propagator relies on the fact that the EOMs obey the Dirac–Frenkel variational principle

$$\langle \delta\Psi|\hat{H} - i\partial_t|\Psi\rangle = 0 \Rightarrow \langle \delta\Psi| \perp \langle \Psi|. \tag{3′}$$

If the EOMs are derived assuming a Hermitian $\hat{H}$, the presence of the CAP may result in the EOMs no longer obeying (3′). Applying the CAP as a mask function circumvents the issue.

IV. RESULTS

We now outline the capabilities of our TD-CIS implementation using He, Ne, and a variety of small molecules: LiH, H_2O, and C_2H_4. In all cases the GAMESS-US [69] electronic structure program was used to compute the initial restricted Hartree–Fock (RHF) molecular orbitals (MOs). Since only the basis set and the corresponding expansion coefficients of the MOs are required as inputs for the TD-CIS computations, any electronic structure program may be used. All the required one- and two-electron matrix elements are then evaluated by a Gaussian integral package internal to the TD-CIS code. The aug-cc-pVTZ basis set was used for each system.

Except for the case of He, the TD-CIS computations were all carried out using continuum grids that extended from -22.5 to 22.5 bohrs in all spatial directions with $270 \times 270 \times 270$ grid points, yielding a spatial step size of $h \approx 0.167$ bohr. The time step in all cases was $\tau = 0.002$ a.u. ≈ 0.05 as.

A. Atoms: Helium and neon

In the case of helium, accurate static-field ionization rates are available in the literature. Scrinzi *et al.* [70], in particular, computed the He ionization rates using a full-dimensional treatment within the exterior complex scaling (ECS) methodology. Jagau [71] used a complex-scaled coupled-cluster

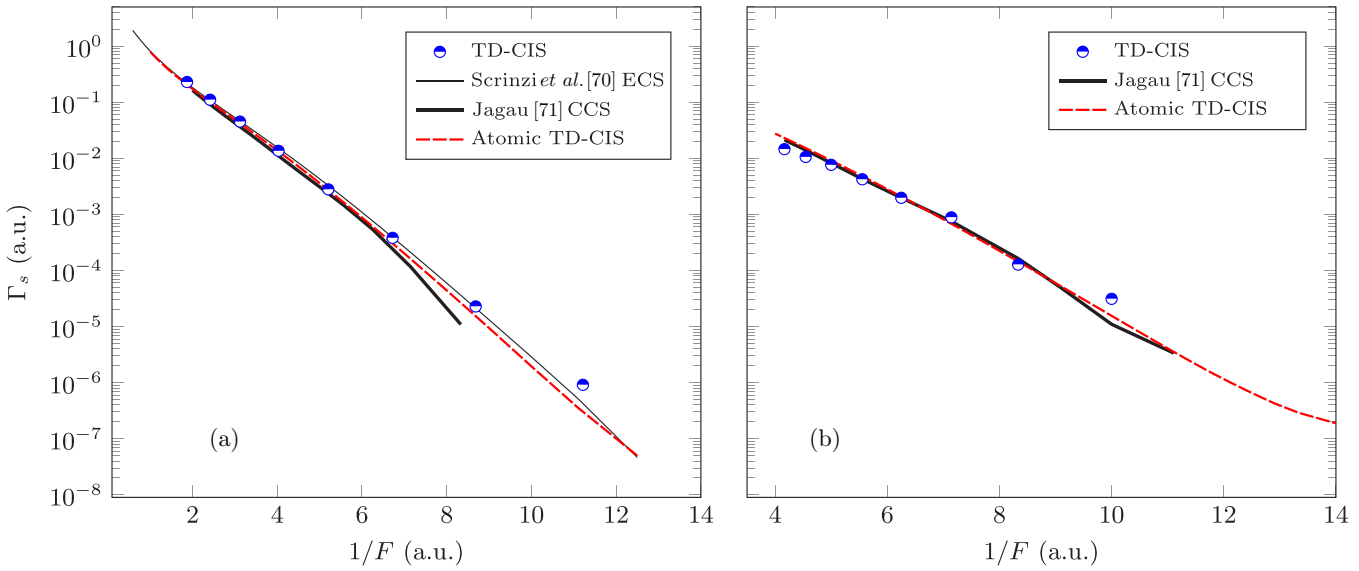

FIG. 1. Static-field ionization rates Γ_s for (a) He and (b) Ne. The rates computed with the current TD-CIS method are compared against the exact results of Scrinzi *et al.* [70], who used a full-dimensional complex scaling method, as well as Jagau [71], who used a complex-scaled coupled-cluster approach. Also shown are the TD-CIS results obtained with the specialization to spherical symmetry (see the following paper [52]).

approach, at various levels of theory for the field-free reference state; for our purpose, the coupled-cluster-singles (CCS) rates are the most relevant. We use these rates as a benchmark to confirm the validity of our TD-CIS implementation. The spatial grid extends from -15 to 15 bohrs, in all spatial directions with $180 \times 180 \times 180$ grid points, yielding a spatial step size $h \approx 0.168$ bohr.

In order to compute the static-field ionization rates within TD-CIS, a time-dependent computation is run with the system initialized in the neutral state. With a static field applied, the time-dependent population of the neutral, $|c_0(t)|^2$, is monitored. After an initial turn-on transient has passed, the long-time behavior of $|c_0(t)|^2$ is fit to an exponential decay ($\sim e^{-\Gamma_s t}$) to extract the static-field ionization rate Γ_s. Figure 1 shows the TD-CIS ionization rates, which are in excellent agreement with those obtained by Scrinzi *et al.* [70], Jagau [71]. At lower intensities, our computational box is not sufficiently large enough to contain the tunnel exit (see the discussion for H_2O below). The apparent ionization rates at these intensities are the upper bound to the true tunneling rate.

B. Convergence

As a test of the convergence of the calculations, we compute the static ionization rates for He for different grid spacings and time steps. We compare with the results from the atomic TD-CIS implementation, which is at the same level of theory and thus serves as our method limit. In Fig. 2 the convergence with respect to the grid spacing is shown. Its behavior is nonuniform, reflecting the underlying complexity of the iterative algorithms. For the different time steps tried, i.e., $\tau \in \{0.001, 0.002, 0.004, 0.008, 0.016\}$ a.u., the change in the error was negligible for all field strengths F and grid spacings h. The convergence with respect to the time step is most likely limited by the tolerance set for the Poisson solver employed for the Coulomb interaction.

C. LiH

The LiH molecule has two occupied orbitals in the RHF neutral ground state. However, only the highest occupied molecular orbital (HOMO) ionizes with non-negligible probability, due to the large binding potential of the HOMO-1. Hence, we treat LiH as a single channel case, with the lower-lying RHF orbital frozen during the computations.

We calculate the half-cycle ionization yield using a smoothed half-cycle pulse defined as

$$F(t) = \begin{cases} 0, & t < 0 \\ F_0 \sin^2(\alpha t), & 0 \leqslant t \leqslant t_{\max}, \\ 0, & t > t_{\max}, \end{cases} \quad \alpha \stackrel{\text{def}}{=} \frac{\omega_L}{\sqrt{2}} \tag{15}$$

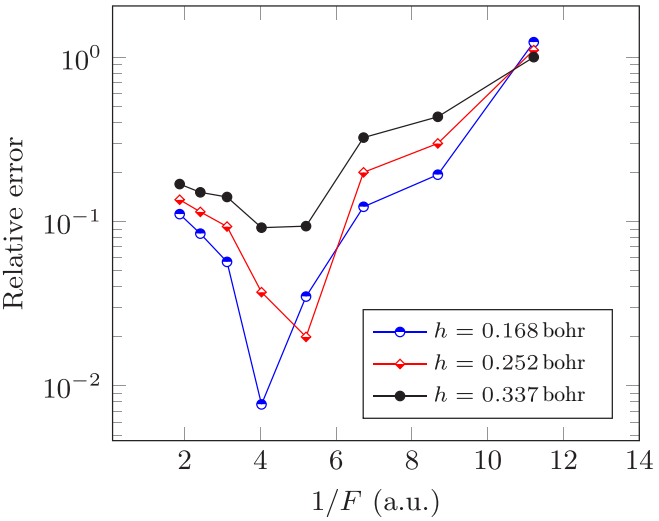

FIG. 2. Relative errors of the He static field ionization rates shown in Fig. 1 with respect to the atomic TD-CIS results, for various grid spacings.

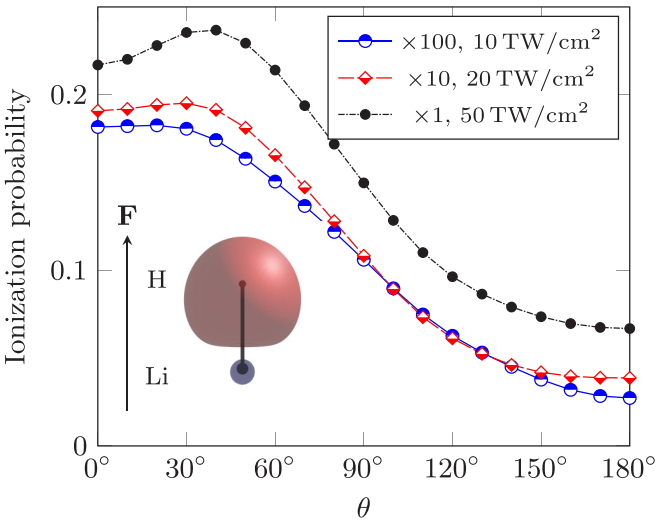

FIG. 3. Angle-dependent half-cycle ionization yields for LiH for intensities of 10 TW/cm^2 (data scaled by 100×), 20 TW/cm^2 (data scaled by 10×), and 50 TW/cm^2. Here θ is the angle between the molecular axis and the electric-field vector of the laser. We clearly see that doubling the intensity ($\sim F_0^2$) increased the ionization probability by more than one order of magnitude. The inset shows the ionizing orbital, along with the electric-field vector **F** for the $\theta = 0$ configuration where the field points from the Li to the H atom.

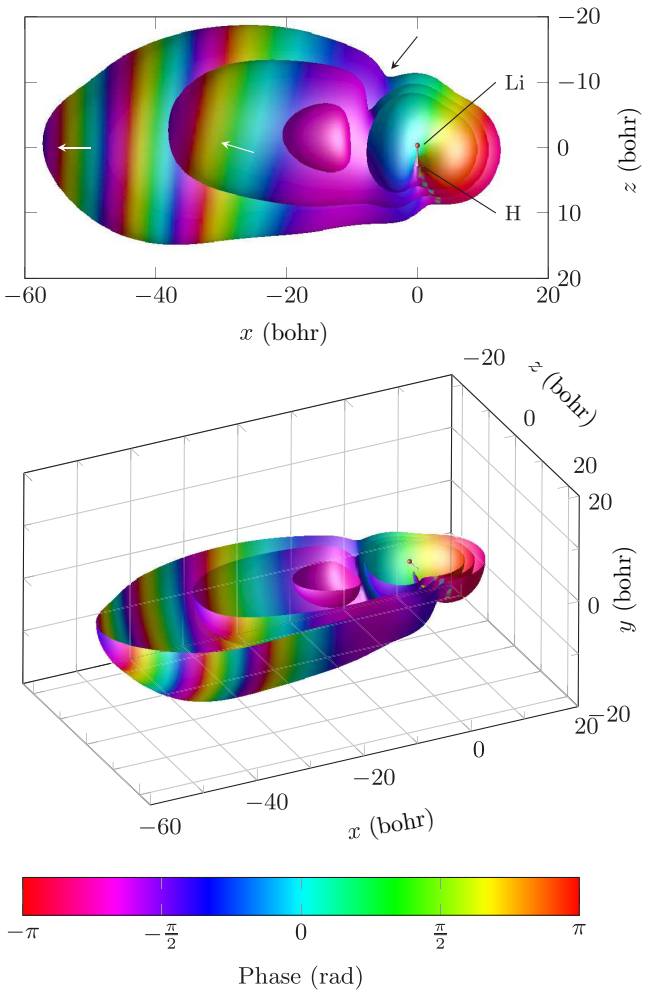

FIG. 4. Continuum electron wave packet after the end of the pulse [$t = t_{\max}$ in (15)] for $\theta = 90°$ and 20 TW/cm^2.

where $t_{\max} = \pi/\alpha$. This pulse shape mimics the high-intensity portion of a half cycle of a laser field with frequency ω_L, but using the smoothed half cycle reduces artifacts that arise from an instantaneous turn-on had just a standard half-cycle field been used instead. For all remaining computations, we use $\omega_L = 0.057$ Ha, which corresponds to an 800-nm laser field. In addition to minimizing the computational load required to compute the ionization compared to that needed for a multicycle pulse, using a half-cycle-type pulse allows us to see the orientation dependence of the ionization yields when ionizing polar molecules like LiH (and H_2O considered below).

The angle-dependent half-cycle ionization yields are presented in Fig. 3 for the laser intensities for a variety of laser intensities. The inset shows the definition of the angle between the molecular axis and the electric field of the ionizing pulse; $\theta = 0$ corresponds to the electric-field vector of the laser pointing from the Li to the H atom. Since the motion of the liberated electron will be opposite to the direction of the electric field, the angle corresponding to the peak of the angle-dependent ionization ($\theta \approx 0$–$45°$) sees the liberated electron escape from the initial HOMO (located on the H atom) across the Li atom.

Figure 4 shows the continuum electron wave packet at the end of the laser pulse, for the case of $\theta = 90°$, i.e., the laser field is perpendicular to the molecular axis. The tunnel barrier is clearly visible around $x \approx -5$ bohr, in that the wave packet appears pinched (marked with a black arrow). The colormap which corresponds to the phase indicates that the wavefront (and hence the direction of travel) right after the tunnel exit is directed upward (smaller value of θ), but after some distance, the electron motion tends to $-90°$, i.e., parallel to $-x$, opposite to the field polarization (marked with white arrows). This agrees with the observation above that the electron preferentially escapes the potential in the vicinity of the Li atom.

D. H_2O

Due to the lower symmetry of H_2O, belonging to the C_{2v} point group, it is not enough to compute the photoionization yields as a function of θ only. We therefore choose a ninth-order Lebedev grid [72] that can represent integrals involving spherical harmonics up to $\ell = \lfloor \frac{9-1}{2} \rfloor = 4$ exactly. From this grid of 38 field orientations, only 16 that are unique with respect to the C_{2v} symmetry are actually computed and then replicated. The resulting yield surface is then transformed to the equivalent expansion in spherical harmonics; the results are shown in Fig. 5. For the three highest occupied molecular orbitals and four different intensities of the driving field, the ionization yields are plotted as a function of the angles θ and ϕ, as well as angle integrated. The same field (15) is used as for LiH, i.e., a half cycle of 800 nm. Additionally, static ionization rates are computed (similarly to He and Ne) orthogonal to the molecular plane, i.e., along the lobes of the HOMO (the x axis), and compared with the CCS results of Jagau [73].

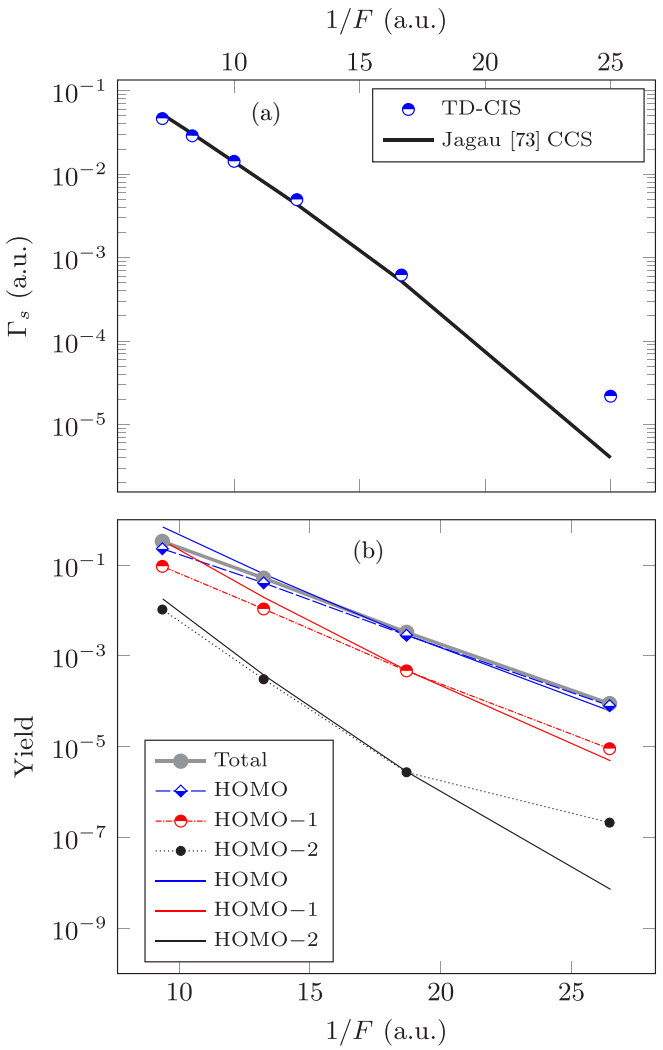

FIG. 5. (a) Static ionization rates of H_2O, orthogonal to the molecular plane, compared with the CCS results of Jagau [73]. (b) Half-cycle intensity-dependent photoionization yield of H_2O, total, as well as resolved on the RHF orbitals. The knee observed at lower intensities for HOMO−2 is a polarization effect (see the text for details). For comparison, the solid lines indicate the ionization yields as predicted by an Keldysh-like theory (16), where only the exponential factor due to the ionization potential of the molecular orbitals and the field strength is considered. These lines have been normalized to the respective TD-CIS results at 100 TW/cm^2.

The dynamic photoionization yields can be compared to tunneling yields estimated from a Keldysh-like [74] formula for the ionization rate

$$w \sim \exp\left[-\frac{1}{3\tilde{\mathcal{E}}}g(\gamma)\right],$$
$$g(\gamma) \stackrel{\text{def}}{=} \frac{3}{2\gamma}\left[\left(1+\frac{1}{2\gamma^2}\right)\operatorname{arcsinh}\gamma - \frac{\sqrt{1+\gamma^2}}{2\gamma}\right], \quad (16)$$

where $\gamma \stackrel{\text{def}}{=} \sqrt{I_\text{p}/2U_\text{p}}$, $\tilde{\mathcal{E}} \stackrel{\text{def}}{=} F[2(2I_\text{p})^{3/2}]^{-1}$, and the estimated ionization yield $y = wt_\text{max}$. We attribute the deviations of the predictions by the tunneling formula from the TD-CIS results to the neglect of many-electron dynamics in the molecule in (16). The nonexponential behavior of the HOMO−2 yield for the smallest intensity is an artifact of limited computational box size. We compute the classical tunnel exit according to

$$r_\text{exit} = \frac{2I_\text{p}}{4F} + \sqrt{\left(\frac{2I_\text{p}}{4F}\right)^2 - \frac{2I_\text{p}}{F}}, \quad (17)$$

where I_p is the magnitude of the orbital energy in Koopman's approximation and $F = \sqrt{I}$ the peak amplitude of the ionizing field. Table I shows the estimated tunnel exits for the three highest occupied molecular orbitals and the various field strengths. For the weakest field, we see that the tunnel exit of the HOMO−2 is very close to the onset of the CAP. This means that in that particular channel, Rydberg states (which extend into the classically forbidden region in the tunnel but not beyond it) incorrectly count towards the photoionization yield, since we compute ionization as loss of norm. Hence, what we observe is a polarization effect, rather than true ionization, for these MOs. Also the angular distribution of the yield for the HOMO−2 is affected by this artifact, resulting in a qualitatively different shape for the lowest intensity. This error decreases with increased box size, at the cost of longer computation times.

TABLE I. Tunnel exit (17) for H_2O. Missing values indicate barrier suppression. The MO energies are given in the second row. The CAP starts at 18.13 bohrs.

Intensity (TW/cm^2)	F (a.u.)	HOMO 0.511 Ha	HOMO−1 0.585 Ha	HOMO−2 0.723 Ha
400	0.107			
200	0.075			6.733
100	0.053	6.727	8.328	11.106
50	0.038	11.100	13.141	16.887

We now turn to the angular distributions of the photoionization yields; as we can see in Fig. 6(a), the MOs are very similar to atomic orbitals (AOs) of p symmetry. The small deviation of the MOs from pure spherical symmetry leads however to drastically different angularly resolved ionization yields, where the electron preferentially leaves the molecule over the O atom, which we attribute primarily to dipole effects. This pattern persists for all intensities, although the HOMO−1 contribution in the direction of the two H atoms does seem to increase slightly with intensity [middle column of Fig. 6(b)]. The nodal planes in the HOMO and HOMO−2 yields are mandated by the C_{2v} symmetry. The observed nodal plane in the HOMO−1 yields is however required by an approximate, higher symmetry, D_{2h}. This serves to further highlight the atomistic nature of the H_2O MOs, which we can quantitatively investigate by computing their overlaps with the p AOs of O (see Table II).

In Fig. 7 the photoionization yields along x for an eight-cycle pulse with a $\sin^2$ envelope and a carrier wavelength of 800 nm are shown. The yields are compared with the results of Benda *et al.* [75] (specifically their coupled model B) and show very good agreement. The discrepancy can

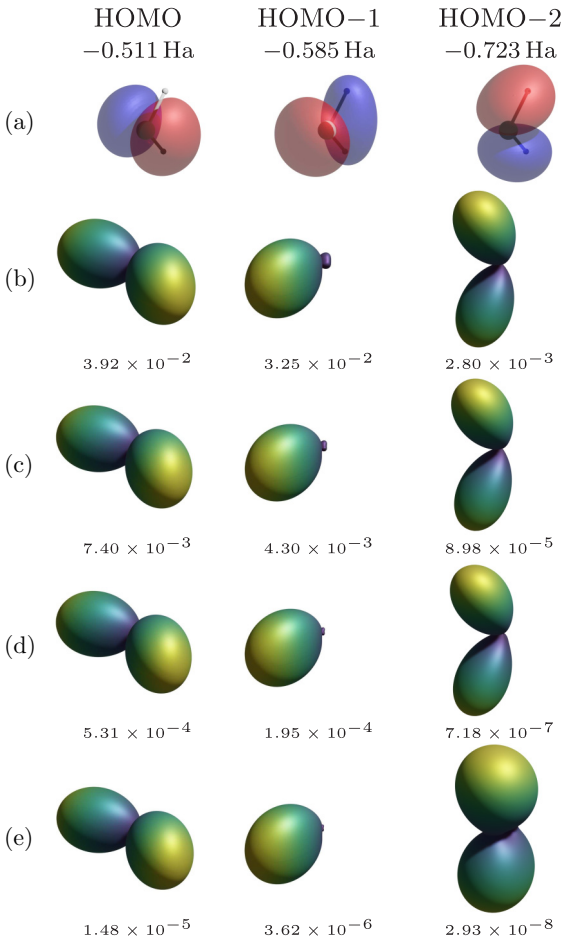

FIG. 6. (a) RHF orbitals of H_2O, along with their angle-resolved ionization yields, for the following intensities: (b) 400 TW/cm^2, (c) 200 TW/cm^2, (d) 100 TW/cm^2, and (e) 50 TW/cm^2. The yields have been normalized to their respective maximum values, indicated below each distribution.

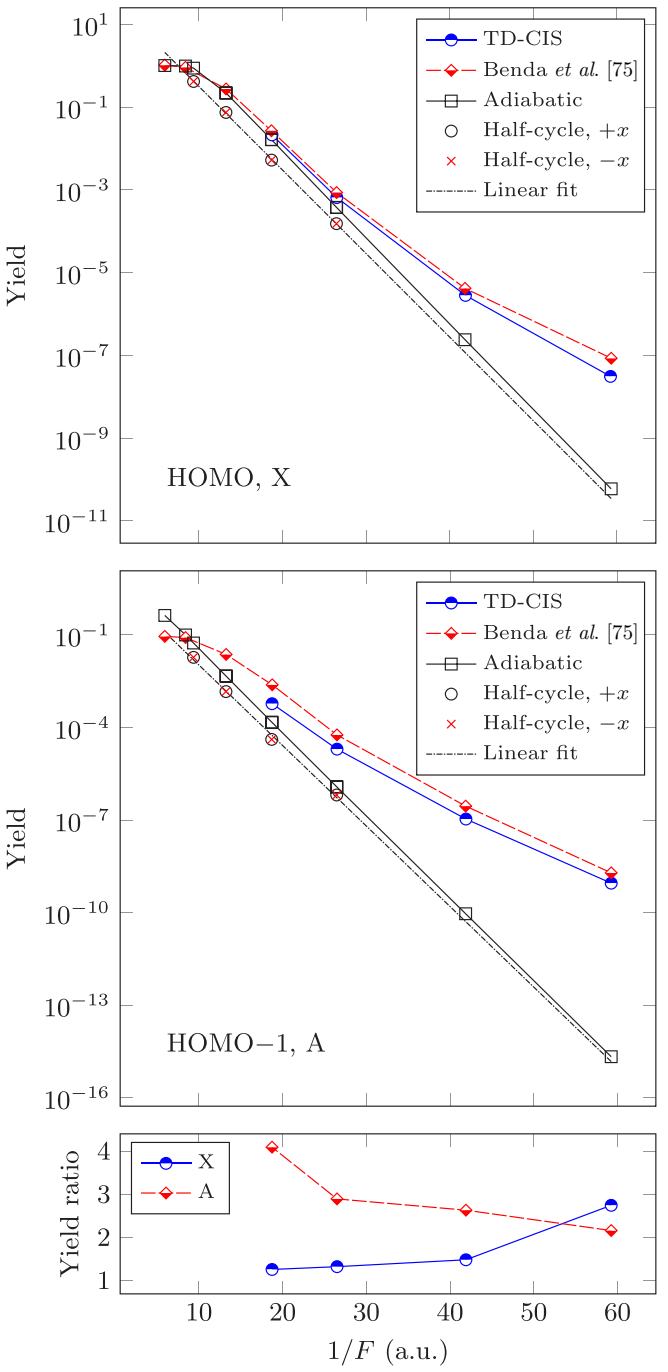

FIG. 7. H_2O yields for ionization from the two highest-lying occupied orbitals using an eight-cycle pulse, as a function of inverse field strength. The yields are compared with the results of Benda *et al.* [75], as well as with an adiabatic estimate (18) formed from the half-cycle yields presented in Fig. 5. The bottom panel shows the ratio between the results of Benda *et al.* [75] and the present work.

be mostly attributed to the difference in ionization potentials; in the present work, the MOs are slightly more bound than in the calculations by Benda *et al.* [75] (13.90 eV vs 13.15 eV for the HOMO and 15.92 eV vs 15.15 eV for the HOMO−1), which has a strong effect due to the exponential sensitivity of strong-field ionization to the ionization potential.

Also shown are the half-cycle yields y_n in Fig. 5(b), along with their logarithms $\log_{10}(y_i)$, which appear to follow a linear trend as a function of the inverse field strength $1/F_n$. We may therefore estimate the eight-cycle yield adiabatically as

$$y = 1 - \exp\left\{-\int_{-\infty}^{\infty} dt\Gamma[F(t)]\right\}$$
$$\approx 1 - \exp\left[-\sum_i \langle\Gamma(F_i)\rangle\right] = 1 - \prod_i [1 - \tilde{y}(F_i)], \quad (18)$$

TABLE II. Overlaps between the molecular orbitals of the H_2O ground state and those of the O ground state. We see that, to a very large degree, the MOs of H_2O are atomistic.

MO	O p_x	O p_y	O p_z
H_2O HOMO	0.995	0.000	0.000
H_2O HOMO−1	0.000	0.000	0.951
H_2O HOMO−2	0.000	0.944	0.000

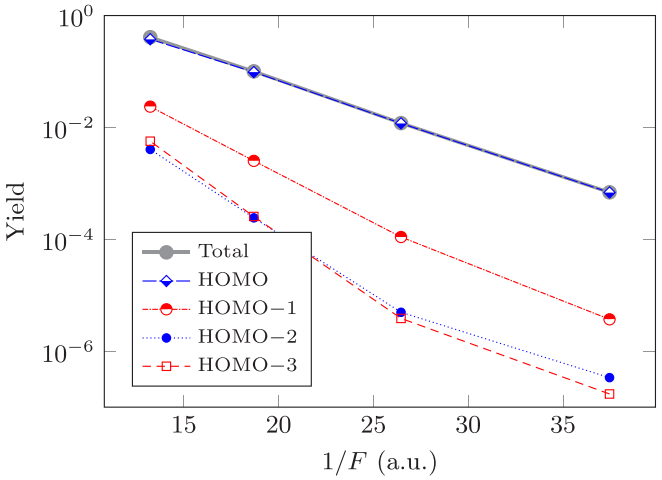

FIG. 8. Intensity-dependent photoionization yield of C_2H_4, total as well as resolved on the RHF orbitals.

where F_i is the peak field amplitude of the ith half cycle and the corresponding yields $\tilde{y}(F_i)$ are found using a linear fit to the half-cycle yields y_n. This estimate of course neglects any cycle-to-cycle effects, which explains its deviation from the true eight-cycle results at lower intensities (higher $1/F$). For higher intensities, the adiabatic results are however in good agreement with the full calculations.

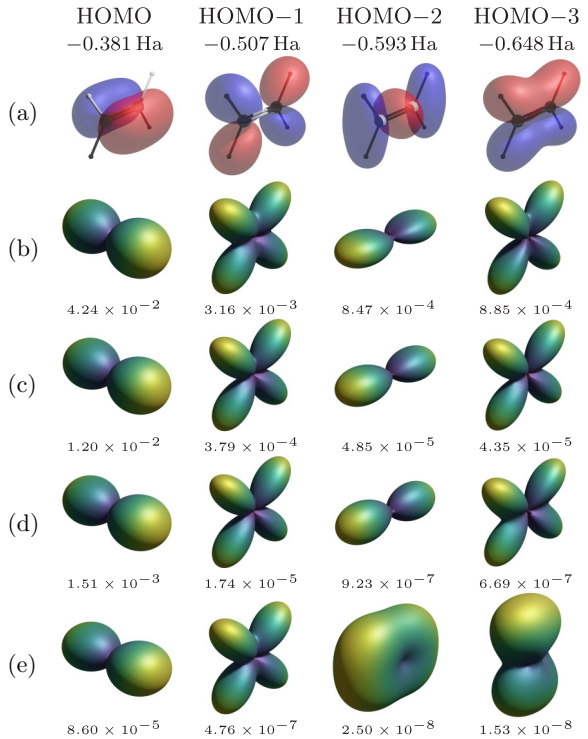

FIG. 9. (a) RHF orbitals of C_2H_4, along with their angle-resolved ionization yields, for the following intensities: (b) 200 TW cm^{-2}, (c) 100 TW cm^{-2}, (d) 50 TW cm^{-2}, and (e) 25 TW cm^{-2}. The yields have been normalized to their respective maximum values, indicated below each distribution.

TABLE III. Tunnel exit (17) for C_2H_4. Missing values indicate barrier suppression. The MO energies are given in the second row. The CAP starts at 18.13 bohrs.

Intensity (TW/cm^2)	F (a.u.)	HOMO 0.381 Ha	HOMO−1 0.507 Ha	HOMO−2 0.593 Ha	HOMO−3 0.648 Ha
200	0.075				5.412
100	0.053		6.636	8.494	9.615
50	0.038	7.347	10.988	13.360	14.858
25	0.027	11.871	16.726	19.997	22.081

E. C_2H_4

Ionization yields are computed similarly to H_2O, as detailed above, but C_2H_4 belonging to the D_{2h} point group has higher symmetry than H_2O and only nine unique field orientations are required. The results are shown in Fig. 8 and the corresponding angular distributions in Fig. 9.

Again, as in the case of H_2O, we find that for the lower intensities, the yields for the HOMO−2 and HOMO−3 deviate from the expected exponential behavior, with a knee observed in the integrated ionization yield and qualitatively different angular distributions [Fig. 9(e)], whereas the HOMO and HOMO−1 follow their respective trends also for the lowest intensity. Table III lists the tunnel exits for the various MOs and intensities, and for the HOMO−2 and HOMO−3 and the lowest intensity, these are well beyond the CAP onset, implying we are measuring mainly a polarization effect.

In Fig. 10 we compare an adiabatic estimation according to (18) of the seven-cycle yield with the results by Krause and Schlegel [17]. Their quoted ionization rates were multiplied by the duration of the pulse [cf. their Eq. (8)] to obtain the yields; we do not find agreement between the different calculations. Extracting the true ionization rates is nontrivial, due to the temporal intensity averaging, which is why we cannot easily compare directly with the half-cycle yields presented in Fig. 8. We also note the experimental work of Talebpour *et al.* [76], the comparison with which would require detailed

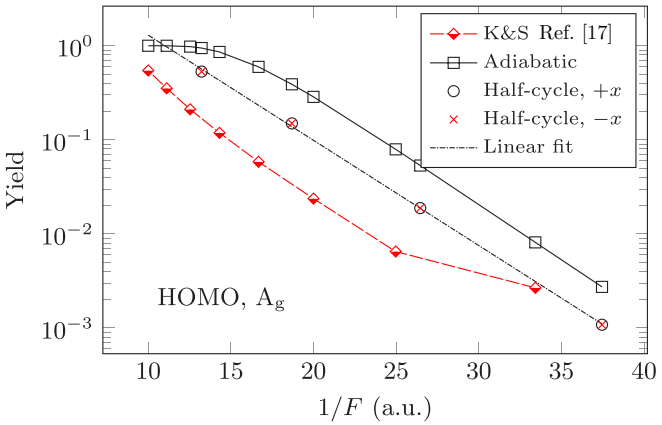

FIG. 10. C_2H_4 adiabatic dynamic yields (18) for a seven-cycle pulse, compared with the results of Krause and Schlegel [17].

knowledge of the experimental conditions, not available to us, as well as extensive simulations.

V. CONCLUSION

We have described an implementation of TD-CIS for small gas-phase molecules, with the continuum electron resolved on a Cartesian grid, which allows an accurate description of the photoelectron in strong-field processes. We applied this method to a few molecules, finding reasonable results for the angularly resolved ionization probability. An implementation of t+iSURF for TD-CIS in the atomic case is presented in the following article [52]; an implementation for the general case is left for future work, which would allow us to efficiently compute photoelectron spectra for various processes of interest.

ACKNOWLEDGMENT

The work of S.C. was supported through scholarship 185-608 from Stiftelsen Olle Engkvist Byggmästare.

[1] F. Krausz and M. Ivanov, Attosecond physics, Rev. Mod. Phys. **81**, 163 (2009).

[2] A. Scrinzi, M. Y. Ivanov, R. Kienberger, and D. M. Villeneuve, Attosecond physics, J. Phys. B **39**, R1 (2006).

[3] O. Smirnova, Y. Mairesse, S. Patchkovskii, N. Dudovich, D. Villeneuve, P. Corkum, and M. Y. Ivanov, High harmonic interferometry of multi-electron dynamics in molecules, Nature (London) **460**, 972 (2009).

[4] H. Soifer, P. Botheron, D. Shafir, A. Diner, O. Raz, B. D. Bruner, Y. Mairesse, B. Pons, and N. Dudovich, Near-Threshold High-Order Harmonic Spectroscopy with Aligned Molecules, Phys. Rev. Lett. **105**, 143904 (2010).

[5] H. J. Wörner, J. B. Bertrand, D. V. Kartashov, P. B. Corkum, and D. M. Villeneuve, Following a chemical reaction using high-harmonic interferometry, Nature (London) **466**, 604 (2010).

[6] H. J. Wörner, J. B. Bertrand, B. Fabre, J. Higuet, H. Ruf, A. Dubrouil, S. Patchkovskii, M. Spanner, Y. Mairesse, V. Blanchet, E. Mével, E. Constant, P. B. Corkum, and D. M. Villeneuve, Conical intersection dynamics in NO_2 probed by homodyne high-harmonic spectroscopy, Science **334**, 208 (2011).

[7] O. Kneller, D. Azoury, Y. Federman, M. Krüger, A. J. Uzan, G. Orenstein, B. D. Bruner, O. Smirnova, S. Patchkovskii, M. Ivanov, and N. Dudovich, A look under the tunnelling barrier via attosecond-gated interferometry, Nat. Photon. **16**, 304 (2022).

[8] J. Itatani, J. Levesque, D. Zeidler, H. Niikura, H. Pépin, J. C. Kieffer, P. B. Corkum, and D. M. Villeneuve, Tomographic imaging of molecular orbitals, Nature (London) **432**, 867 (2004).

[9] M. Spanner, O. Smirnova, P. B. Corkum, and M. Y. Ivanov, Reading diffraction images in strong field ionization of diatomic molecules, J. Phys. B **37**, L243 (2004).

[10] S. N. Yurchenko, S. Patchkovskii, I. V. Litvinyuk, P. B. Corkum, and G. L. Yudin, Laser-Induced Interference, Focusing, and Diffraction of Rescattering Molecular Photoelectrons, Phys. Rev. Lett. **93**, 223003 (2004).

[11] M. Meckel, D. Comtois, D. Zeidler, A. Staudte, D. Pavicic, H. C. Bandulet, H. Pepin, J. C. Kieffer, R. Dorner, D. M. Villeneuve, and P. B. Corkum, Laser-induced electron tunneling and diffraction, Science **320**, 1478 (2008).

[12] Y. Huismans, A. Rouzee, A. Gijsbertsen, J. H. Jungmann, A. S. Smolkowska, P. S. W. M. Logman, F. Lepine, C. Cauchy, S. Zamith, T. Marchenko, J. M. Bakker, G. Berden, B. Redlich, A. F. G. van der Meer, H. G. Muller, W. Vermin, K. J. Schafer, M. Spanner, M. Y. Ivanov, O. Smirnova *et al.*, Time-resolved holography with photoelectrons, Science **331**, 61 (2010).

[13] T. Klamroth, Laser-driven electron transfer through metal-insulator-metal contacts: Time-dependent configuration interaction singles calculations for a jellium model, Phys. Rev. B **68**, 245421 (2003).

[14] P. Krause, T. Klamroth, and P. Saalfrank, Time-dependent configuration-interaction calculations of laser-pulse-driven many-electron dynamics: Controlled dipole switching in lithium cyanide, J. Chem. Phys. **123**, 074105 (2005).

[15] H. B. Schlegel, S. M. Smith, and X. Li, Electronic optical response of molecules in intense fields: Comparison of TD-HF, TD-CIS, and TD-CIS(D) approaches, J. Chem. Phys. **126**, 244110 (2007).

[16] P. Krause, J. A. Sonk, and H. B. Schlegel, Strong field ionization rates simulated with time-dependent configuration interaction and an absorbing potential, J. Chem. Phys. **140**, 174113 (2014).

[17] P. Krause and H. B. Schlegel, Strong-field ionization rates of linear polyenes simulated with time-dependent configuration interaction with an absorbing potential, J. Chem. Phys. **141**, 174104 (2014).

[18] P. Krause and H. B. Schlegel, Angle-dependent ionization of small molecules by time-dependent configuration interaction and an absorbing potential, J. Phys. Chem. Lett. **6**, 2140 (2015).

[19] P. Saalfrank, F. Bedurke, C. Heide, T. Klamroth, S. Klinkusch, P. Krause, M. Nest, and J. C. Tremblay, *Chemical Physics and Quantum Chemistry* (Elsevier, Amsterdam, 2020), pp. 15–50.

[20] N. Rohringer, A. Gordon, and R. Santra, Configuration-interaction-based time-dependent orbital approach for *ab initio* treatment of electronic dynamics in a strong optical laser field, Phys. Rev. A **74**, 043420 (2006).

[21] L. Greenman, P. J. Ho, S. Pabst, E. Kamarchik, D. A. Mazziotti, and R. Santra, Implementation of the time-dependent configuration-interaction singles method for atomic strong-field processes, Phys. Rev. A **82**, 023406 (2010).

[22] F. Zapata, J. Vinbladh, A. Ljungdahl, E. Lindroth, and J. M. Dahlström, Relativistic time-dependent configuration-interaction singles method, Phys. Rev. A **105**, 012802 (2022).

[23] E. Runge and E. K. U. Gross, Density-Functional Theory for Time-Dependent Systems, Phys. Rev. Lett. **52**, 997 (1984).

[24] D. A. Telnov and S.-I. Chu, Floquet formulation of time-dependent density functional theory, Chem. Phys. Lett. **264**, 466 (1997).

[25] D. A. Telnov and S.-I. Chu, Generalized Floquet theoretical formulation of time-dependent density functional theory

for many-electron systems in multicolor laser fields, Int. J. Quantum Chem. **69**, 305 (1998).

[26] U. De Giovannini, D. Varsano, M. A. L. Marques, H. Appel, E. K. U. Gross, and A. Rubio, *Ab initio* angle- and energy-resolved photoelectron spectroscopy with time-dependent density-functional theory, Phys. Rev. A **85**, 062515 (2012).

[27] H.-D. Meyer, U. Manthe, and L. Cederbaum, The multi-configurational time-dependent Hartree approach, Chem. Phys. Lett. **165**, 73 (1990).

[28] M. Beck, A. Jäckle, G. Worth, and H.-D. Meyer, The multiconfiguration time-dependent Hartree (MCTDH) method: A highly efficient algorithm for propagating wavepackets, Phys. Rep. **324**, 1 (2000).

[29] S. Kvaal, Multiconfigurational time-dependent Hartree method to describe particle loss due to absorbing boundary conditions, Phys. Rev. A **84**, 022512 (2011).

[30] J. Zanghellini, M. Kitzler, C. Fabian, T. Brabec, and A. Scrinzi, An MCTDHF approach to multi-electron dynamics in laser fields, Laser Phys. **13**, 1064 (2003).

[31] J. Zanghellini, M. Kitzler, T. Brabec, and A. Scrinzi, Testing the multi-configuration time-dependent Hartree–Fock method, J. Phys. B **37**, 763 (2004).

[32] J. Zanghellini, M. Kitzler, Z. Zhang, and T. Brabec, Multi-electron dynamics in strong laser fields, J. Mod. Opt. **52**, 479 (2005).

[33] M. Nest, T. Klamroth, and P. Saalfrank, The multiconfiguration time-dependent Hartree–Fock method for quantum chemical calculations, J. Chem. Phys. **122**, 124102 (2005).

[34] D. Hochstuhl and M. Bonitz, Two-photon ionization of helium studied with the multiconfigurational time-dependent Hartree–Fock method, J. Chem. Phys. **134**, 084106 (2011).

[35] T. Kato and H. Kono, Time-dependent multiconfiguration theory for electronic dynamics of molecules in an intense laser field, Chem. Phys. Lett. **392**, 533 (2004).

[36] T. Sato and K. L. Ishikawa, Time-dependent complete-active-space self-consistent-field method for multielectron dynamics in intense laser fields, Phys. Rev. A **88**, 023402 (2013).

[37] M. Spanner and S. Patchkovskii, One-electron ionization of multielectron systems in strong nonresonant laser fields, Phys. Rev. A **80**, 063411 (2009).

[38] D. Hochstuhl and M. Bonitz, Time-dependent restricted-active-space configuration-interaction method for the photoionization of many-electron atoms, Phys. Rev. A **86**, 053424 (2012).

[39] T. Sato and K. L. Ishikawa, Time-dependent multiconfiguration self-consistent-field method based on the occupation-restricted multiple-active-space model for multielectron dynamics in intense laser fields, Phys. Rev. A **91**, 023417 (2015).

[40] C. Huber and T. Klamroth, Explicitly time-dependent coupled cluster singles doubles calculations of laser-driven many-electron dynamics, J. Chem. Phys. **134**, 054113 (2011).

[41] S. Kvaal, *Ab initio* quantum dynamics using coupled-cluster, J. Chem. Phys. **136**, 194109 (2012).

[42] T. Sato, H. Pathak, Y. Orimo, and K. L. Ishikawa, Communication: Time-dependent optimized coupled-cluster method for multielectron dynamics, J. Chem. Phys. **148**, 051101 (2018).

[43] M. Ruberti, V. Averbukh, and P. Decleva, B-spline algebraic diagrammatic construction: Application to photoionization cross-sections and high-order harmonic generation, J. Chem. Phys. **141**, 164126 (2014).

[44] M. Ruberti, R. Yun, K. Gokhberg, S. Kopelke, L. S. Cederbaum, F. Tarantelli, and V. Averbukh, Total photoionization cross-sections of excited electronic states by the algebraic diagrammatic construction-Stieltjes–Lanczos method, J. Chem. Phys. **140**, 184107 (2014).

[45] M. Ruberti, Restricted correlation space B-spline ADC approach to molecular ionization: Theory and applications to total photoionization cross-sections, J. Chem. Theory Comput. **15**, 3635 (2019).

[46] Z. Mašín, J. Benda, J. D. Gorfinkiel, A. G. Harvey, and J. Tennyson, UKRmol+: A suite for modelling electronic processes in molecules interacting with electrons, positrons and photons using the *R*-matrix method, Comput. Phys. Commun. **249**, 107092 (2020).

[47] A. C. Brown, G. S. Armstrong, J. Benda, D. D. Clarke, J. Wragg, K. R. Hamilton, Z. Mašín, J. D. Gorfinkiel, and H. W. van der Hart, RMT: *R*-matrix with time-dependence. solving the semi-relativistic, time-dependent Schrödinger equation for general, multielectron atoms and molecules in intense, ultrashort, arbitrarily polarized laser pulses, Comput. Phys. Commun. **250**, 107062 (2020).

[48] K. Ishikawa and T. Sato, A review on *ab initio* approaches for multielectron dynamics, IEEE J. Sel. Top. Quantum Electron. **21**, 8700916 (2015).

[49] G. S. J. Armstrong, M. A. Khokhlova, M. Labeye, A. S. Maxwell, E. Pisanty, and M. Ruberti, Dialogue on analytical and *ab initio* methods in attoscience, Eur. Phys. J. D **75**, 209 (2021).

[50] P.-O. Löwdin, Quantum theory of many-particle systems. I. Physical interpretations by means of density matrices, natural spin-orbitals, and convergence problems in the method of configurational interaction, Phys. Rev. **97**, 1474 (1955).

[51] R. Car and M. Parrinello, Unified Approach for Molecular Dynamics and Density-Functional Theory, Phys. Rev. Lett. **55**, 2471 (1985).

[52] S. Carlström, M. Bertolino, J. M. Dahlström, and S. Patchkovskii, General time-dependent configuration-interaction singles. II. Atomic case, following paper, Phys. Rev. A **106**, 042806 (2022).

[53] A. Scrinzi, t-SURFF: Fully differential two-electron photoemission spectra, New J. Phys. **14**, 085008 (2012).

[54] Y. Orimo, T. Sato, and K. L. Ishikawa, Application of the time-dependent surface flux method to the time-dependent multiconfiguration self-consistent-field method, Phys. Rev. A **100**, 013419 (2019).

[55] R. L. Martin and D. A. Shirley, Theory of core-level photoemission correlation state spectra, J. Chem. Phys. **64**, 3685 (1976).

[56] B. T. Pickup, On the theory of fast photoionization processes, Chem. Phys. **19**, 193 (1977).

[57] Y. Öhrn and G. Born, in *Advances in Quantum Chemistry*, edited by P.-O. Löwdin (Elsevier, Amsterdam, 1981), vol. 13, pp. 1–88.

[58] S. Patchkovskii, Z. Zhao, T. Brabec, and D. M. Villeneuve, High Harmonic Generation and Molecular Orbital Tomography in Multielectron Systems: Beyond the Single Active Electron Approximation, Phys. Rev. Lett. **97**, 123003 (2006).

[59] L. Tao and A. Scrinzi, Photo-electron momentum spectra from minimal volumes: The time-dependent surface flux method, New J. Phys. **14**, 013021 (2012).

[60] F. Morales, T. Bredtmann, and S. Patchkovskii, iSURF: A family of infinite-time surface flux methods, J. Phys. B **49**, 245001 (2016).

[61] N. Moiseyev, *Non-Hermitian Quantum Mechanics* (Cambridge University Press, Cambridge, 2011).

[62] Y. Saad and M. H. Schultz, GMRES: A generalized minimal residual algorithm for solving nonsymmetric linear systems, SIAM J. Sci. Stat. Comput. **7**, 856 (1986).

[63] M. Wolfsberg, Dipole velocity and dipole length matrix elements in π electron systems and configuration interaction, J. Chem. Phys. **23**, 793 (1955).

[64] D. H. Kobe, Gauge-invariant resolution of the controversy over length versus velocity forms of the interaction with electric dipole radiation, Phys. Rev. A **19**, 205 (1979).

[65] T. Sato, T. Teramura, and K. Ishikawa, Gauge-invariant formulation of time-dependent configuration interaction singles method, Appl. Sci. **8**, 433 (2018).

[66] D. M. Young, Jr., Iterative methods for solving partial difference equations of elliptic type, Ph.D. thesis, Harvard University, 1950.

[67] S. P. Frankel, Convergence rates of iterative treatments of partial differential equations, Math. Tables Aids Comput. **4**, 65 (1950).

[68] D. E. Manolopoulos, Derivation and reflection properties of a transmission-free absorbing potential, J. Chem. Phys. **117**, 9552 (2002).

[69] M. W. Schmidt, K. K. Baldridge, J. A. Boatz, S. T. Elbert, M. S. Gordon, J. H. Jensen, S. Koseki, N. Matsunaga, K. A. Nguyen, S. Su, T. L. Windus, M. Dupuis, and J. A. Montgomery, General atomic and molecular electronic structure system, J. Comput. Chem. **14**, 1347 (1993).

[70] A. Scrinzi, M. Geissler, and T. Brabec, Ionization Above the Coulomb Barrier, Phys. Rev. Lett. **83**, 706 (1999).

[71] T.-C. Jagau, Investigating tunnel and above-barrier ionization using complex-scaled coupled-cluster theory, J. Chem. Phys. **145**, 204115 (2016).

[72] V. Lebedev, Values of the nodes and weights of ninth to seventeenth order Gauss–Markov quadrature formulae invariant under the octahedron group with inversion, USSR Comput. Math. Math. Phys. **15**, 44 (1975).

[73] T.-C. Jagau, Coupled-cluster treatment of molecular strong-field ionization, J. Chem. Phys. **148**, 204102 (2018).

[74] L. V. Keldysh, Ionization in the field of a strong electromagnetic wave, J. Exp. Theor. Phys. **20**, 1307 (1965).

[75] J. Benda, J. D. Gorfinkiel, Z. Mašín, G. S. J. Armstrong, A. C. Brown, D. D. A. Clarke, H. W. van der Hart, and J. Wragg, Perturbative and nonperturbative photoionization of H_2 and H_2O using the molecular *R*-matrix-with-time method, Phys. Rev. A **102**, 052826 (2020).

[76] A. Talebpour, A. Bandrauk, J. Yang, and S. Chin, Multiphoton ionization of inner-valence electrons and fragmentation of ethylene in an intense Ti:sapphire laser pulse, Chem. Phys. Lett. **313**, 789 (1999).